Fast and accurate T$_2$ mapping using Bloch simulations and low-rank plus sparse matrix decomposition

Grzeda Daniel [a], Galun Meirav [b], Omer Noam [a], Blumenfeld-Katzir Tamar [a], Radunsky Dvir [a], Otazo Ricardo [c], Ben-Eliezer Noam [a,d,e,*]

[a] Department of Biomedical Engineering, Tel-Aviv University, Tel Aviv, Israel
[b] Department of Computer Science and Applied Mathematics, Weitzman Institute of Science, Rehovot, Israel
[c] Departments of Medical Physics and Radiology, Memorial Sloan Kettering Cancer Center, New York, NY 10016, USA
[d] Sagol School of Neuroscience, Tel-Aviv University, Tel-Aviv, Israel
[e] Center for Advanced Imaging Innovation and Research (CAI2R), New-York University Langone Medical Center, New York, NY 10016, USA

ARTICLE INFO

ABSTRACT

Purpose: MRI's T$_2$ relaxation time is one of the key contrast mechanisms for clinical diagnosis and prognosis of pathologies. Mapping this relaxation time, however, involves extensive scan times, which are needed to collect quantitative data, thereby impeding its integration into clinical routine. This study employs a low-rank plus sparse (**L + S**) signal decomposition approach in order to reconstruct accurate T$_2$-maps from highly under-sampled multi-echo spin-echo (**MESE**) MRI data.
Methods: Two new algorithms are presented: the first uses standard L + S approach, where both *L* and *S* are iteratively updated. The second technique, dubbed SPArse and fixed RanK (**SPARK**), uses a fixed-rank *L*, under the assumption that most MESE information is found in the *L* component and that this rank can be pre-calculated. The utility of these new techniques is demonstrated on in vivo brain and calf data at x2 to x6 acceleration factors.
Results: Accelerated T$_2$ maps showed improved accuracy compared to fully sampled ground truth maps, when using L + S and SPARK techniques vis-à-vis standard GRAPPA acceleration.
Conclusion: SPARK provides accurate T$_2$ maps with increased robustness to the selection of reconstruction parameters making it suitable to a wide range of applications and facilitating the use of quantitative T$_2$ information in clinical settings.

1. Introduction

MRI's transverse (**T$_2$**) relaxation time is one of the most highly utilized contrast mechanisms for noninvasive diagnosis and prognosis of pathologies. Radiologic interpretation of T$_2$-weighted images is typically done in a visually qualitative manner [1–3], which may lead to protocol- and observer-dependent interpretation and preventing standardized diagnosis. Quantitative T$_2$ mapping (**qT$_2$**) is showing increased clinical merit including the detection and characterization of carcinoma and prostate lesions [4,5], assessment of musculoskeletal pathologies [6–9], diagnosis of ischemic stroke [10], evaluation of cognitive impairment in neurodegenerative diseases [11], and the assessment of acute coronary syndrome and myocardial edema [12,13].

Notwithstanding the popularity of quantitative MRI, qT$_2$ is still not being routinely used in clinical settings due to the challenges of reliably quantifying this relaxation time. These include the extensive scan times associated with single spin-echo acquisitions [1,14], and the contamination of rapid multi echo spin echo (**MESE**) protocols by stimulated and indirect echoes [1,15]. Simplistic exponential fitting of MESE data results in significant overestimation of T$_2$ values [16,17] – a bias which is, moreover, not constant and depends on the scanner and scan setting being used [1,14,16,17].

Several techniques have been developed to improve the accuracy of T$_2$ mapping while maintaining a reasonable acquisition times. Schmitt et al used Inversion Recovery TrueFISP to calculate T$_1$, T$_2$ and proton density (**PD**) from a single temporal signal [18], while DESPOT2 can estimate T$_2$ values in clinically acceptable scan times from only two images acquired with different flip angles and a constant TR [19]. Both IR-TrueFISP and DESPOT2 are based on steady state free precession (**SSFP**) acquisition schemes, which exhibit sensitivity to main field (B$_0$)

---

* Corresponding author at: Department of Biomedical Engineering, Tel Aviv University, Tel Aviv 6997801, Israel.
E-mail address: noambe@tauex.tau.ac.il (B.-E. Noam).

inhomogeneities and reduced T_2 encoding quality vs. spin-echo based protocols [15]. The Extended Phase Graph (**EPG**) algorithm was developed particularly for MESE protocols aiming to track all the coherence pathways that contribute to each echo [20], while also accounting for imperfect slice profile [15]. Another quantitative technique is magnetic resonance fingerprinting, used for mapping multiple parameters including T_1, T_2, and PD. This technique uses a pseudorandomized acquisition to generate a signal fingerprint, followed by fitting of all the parameters encoded in the signal by matching it to a precalculated dictionary of theoretical signal curves [21].

This study uses the echo modulation curve (**EMC**) technique [22], which is part of the family of dictionary matching approaches. This technique relies on full Bloch simulations of the MESE pulse sequence, to provide accurate and reproducible qT_2 values, while paying particular attention to signal variations across different scan settings. By tailoring the fitting process to the specific RF and gradient pulses in the protocol timing diagram, the EMC technique is able to produce values that remain stable across scanners and scan settings [1,11,23]. Previous reports have shown the advantage of Bloch-based fitting approach vs. EPG based mapping for extracting reliable qT_2 values at clinical time scales [16,24,25].

Notwithstanding the accuracy of the EMC technique, MESE acquisitions are still relatively long compared to simple T_2-weighted protocols such as FLAIR, with typical scan times ranging around 6–11 min for full brain coverage using standard x2 acceleration. Further acceleration is therefore needed in order to use qT_2 in clinical routine. This can be achieved by further undersampling the phase encoded dimension of the images' k-space, together with designated data-reconstruction techniques like SENSE or GRAPPA [26,27]. These exploit the correlations between multicoil data to remove undersampling related aliasing and reach clinically feasible scan times within moderate acceleration factors (typically $R = 2$). The framework of compressed sensing (**CS**) has further potential for accelerating data acquisition [28,29]. According to CS theory, fully sampled data can be recovered from randomly undersampled subset of k-space lines by relying on the fact that the data is sparse in some domain [29]. Global and Local Low Rank models have been previously proposed for model-free reconstruction of dynamic MRI data and for model-free rapid T_2 mapping [30,31]. These methods exploit the strong correlations of the data in the temporal domain, reflected as a low rank property, and are helpful in cases where an analytic signal model cannot be applied for reconstruction. Zhao et al. enforced low-rankness by setting a fixed and low rank for the data using factorization of two low-rank matrices in addition to a finite difference constraint along the spatial and temporal domains in order to reduce aliasing-related noise artifacts [32]. Still, all the above techniques rely on a theoretical exponential signal model, and do not account for the empiric distortions of MESE signals due to stimulated echoes.

An alternative approach to exploit low-rankness is the Low Rank + Sparse (*L* + *S*) decomposition, which was recently proposed for accelerating dynamic MRI applications [33]. This approach models the acquired data as the superposition of a low rank component (*L*) and a sparse component (*S*), thereby improving the performance of classical principal component analysis (**PCA**). The temporally correlated background is modeled in *L*, while the dynamic information is modeled by *S* and superimposed on the background. Using L + S decomposition for dynamic MRI data showed superior compressibility compared to the use of only sparse or only low-rank models [33]. A variant on L + S was presented by Weizman et al., where the rank of the reconstructed *L* component was constrained to a predefined value that is meaningful with respect to the underlying data, and the reconstructed *S* component was constrained to be periodic or sparse in the Fourier Transform (**FT**) domain [34].

This study presents two variants of L + S based algorithms, designed to reconstruct T_2 relaxation maps from highly undersampled data. The first uses the standard L + S approach, where both *L* and *S* are iteratively updated. The second, which is called SPArse and fixed RanK (**SPARK**),

uses a fixed-rank *L* determined by the EMC signal model [1]. The pair of new reconstruction techniques was applied on brain and calf data, allowing the ability to reach high acceleration factors with negligible compromise on the T_2 mapping accuracy.

2. Theory

The EMC technique models MESE T_2 decay curves using Bloch simulations that are tailored to the specific pulse sequence being employed. Specifically, the simulations incorporate the exact RF pulse shapes, gradient waveforms, and timing diagram to generate a theoretical EMC curve for each set of experimental parameters. Simulations are then repeated for a range of T_2 and transmit field (B_1^+) inhomogeneity values, ultimately generating a dictionary of EMCs, each associated with a unique $[B_1^+,T_2]$ pair. The dictionary is generated once as a preprocessing step, while the T_2 maps are constructed by matching the experimental decay curve at each voxel to the set of simulated EMC curves and finding the curve with the minimal l_2-norm difference, yielding a single $[B_1^+,T_2]$ pair per voxel [1].

The L + S matrix decomposition is an effective tool for foreground / background separation. The reconstruction of a time-series of undersampled k-space data is given by the following optimization problem:

$$\widehat{L}, \widehat{S} = \frac{1}{2}\|y - E(X)\|_2^2 + \lambda_L \|L\|_* + \lambda_S \|TS\|_1 \ s.t. X = L + S \qquad (1)$$

Here, $y \in \mathbb{C}^{N_{kx}N_{ky}N_{echoes}N_{coils}}$ denotes the vectorized multicoil k-space data; $E = UFC$ is the accelerated acquisition operator with undersampling pattern *U*, 2D-Fourier transform *F* and coil sensitivity *C*; $X = L + S \in \mathbb{R}^{N_x N_y \times N_{echoes}}$ is the decomposition of the underlying anatomy into a low-rank component *L* and sparse component *S* under the transform domain *TS*. The reconstructed data *X* is arranged so that its nth column is a vectorization of the image from the nth echo ($n = 1, \ldots, N_{echoes}$). Two regularization terms are introduced to enforce the low rankness of *L* and the sparsity of *S*. The first is the nuclear norm of *L*, denoted by $\|L\|_*$, and defined as the sum of its singular values, $\|L\|_* = \sum_{i=1}^{min(N_xN_y,N_{echoes})}\sigma_i$. The second regularization term is $\|TS\|_1$ which ensures the sparsity of *S*. The transformation *T* can be tailored to the specific application at hand, e.g., FT for temporally periodic cardiac MRI data [33]. The regularization weights λ_L and λ_S adjust the tradeoff between data consistency and the above two priors. Further details about the encoding operator *E* are found in Appendix A.

Unlike perfusion or cardiac cine data, where signal variations are localized to a certain time window or spatial region [33], MESE signals are dominated by a low-rank relaxation pattern [31], namely, a temporal decay curve which behaves relatively similar across the entire anatomy, with relatively small variations between the signals belonging to different T_2 values. These observations imply that most of the relaxation data in MESE signals is stored in the *L* component, while the *S* component carries natural inter-scan signal variations related to thermal noise and undersampling-related artifacts.

Analysis of a typical EMC dictionary shows that accurate T_2 maps can be achieved using only a small number of singular vectors from the SVD decomposition of the EMC dictionary (Fig. S1). Practical limitations like noise, motion, coil sensitivities, and others may add incoherent noise, increasing the rank of the acquired signal above the theoretical value expected from a dictionary of EMC curves. Another property of experimental MESE signal decay curves (EMCs) is that they exhibit no periodic component [34]. We thus employed the identity operator *I* as the sparsifying transform of *S* to reduce the influence of aliasing and noise, rather than a temporal FT (which was previously used to analyze cardiac data), assuming *S* is already sparse in the image domain. Based on these observations, we can formulate a new optimization problem named SPARK, which extends the L + S method by constraining the low-rank to a value [34] and using the identity transform instead of FT:

$$\widehat{L}, \widehat{S} = \frac{1}{2}\|y - E(X)\|_2^2 + \lambda_S \|S\|_1 \ s.t. X = L + S, rank(L) = r \quad (2)$$

The SPARK algorithm is delineated in Algorithm 1 and is solved in a three-step iterative process. First, initial solutions X_0 and S_0 are chosen. At each iteration, L_k is estimated using the Iterative Hard Thresholding algorithm [34,35], consisting of Singular Value Soft Thresholding (**SVT**) with parameter $\lambda_L \bullet \sigma_{r+1}$ and followed by truncating the rank to a fixed value r. Then, S_k is estimated by soft thresholding with weight λ_S. The soft thresholding operator is given by Λ_λ:

$$\Lambda_\lambda(x) = \frac{x}{|x|} \bullet max(0, |x| - \lambda) \quad (3)$$

Finally, data consistency is applied in a gradient descent step with step size t. The algorithm repeats until a maximum number of iterations is performed or until the relative change in the solution is smaller than ε [33]. A constant value of $t = 1$ can be used given the spectral norm of E, defined by its largest singular value, which is <1. This is achieved by dividing the elements of F by $\sqrt{N_x N_y}$ and coil profiles C by their maximum magnitude [33]. Once fully sampled images are reconstructed, the EMC algorithm is used to generate quantitative T_2 maps [1].

Algorithm 1

1. Initialize: $S_{k=0} = 0, \ X_{k=0} = L_{k=0} = E^H(y)$
2. Iterate for $k = 1, ..., k_{max}$ or until $\frac{\|L_k + S_k - (L_{k-1} + S_{k-1})\|_2}{\|L_{k-1} + S_{k-1}\|_2} \leq \varepsilon$
2.1 *L*-Step
$U\Sigma V^H = SVD(L_{k-1} - tE^H(E(L_{k-1} + S_{k-1}) - y))$
$\widehat{\Sigma} = \{\Lambda_{\lambda_L \cdot \sigma_{r+1}}(\Sigma_{jj}) \quad j \leq r \ 0, j > r$
$L_k = U\widehat{\Sigma}V^H$
2.2 *S*-Step
$S_k = \Lambda_{\lambda_S}(S_{k-1} - tE^H(E(L_{k-1} + S_{k-1}) - y))$
2.3 Data consistency step
$X_k = L_k + S_k - tE^H(E(L_k + S_k) - y)$
y Multicoil undersampled *k-t* data.
E Space-time multicoil encoding operator.
S_k, L_k The sparse and low-rank components estimated at the kth iteration.
X_k The underlying image estimated at the kth iteration.
SVD   Singular Value Decomposition.
Λ_λ Soft-thresholding operator with parameter λ.
t Gradient-step size in the gradient descent iteration.
Stop condition is set by the maximum allowed number of iterations k_{max} and tolerance ε.

3. Methods

3.1. MRI scans

MRI scans of the brains ($N = 3$) and calf (N = 1) of four healthy volunteers were performed on a human 3 T Siemens Magnetom Prisma scanner (Siemens Healthineers). All scans were approved by the local institutional review board and after obtaining written informed consent. Experimental protocols involved a standard MESE scan [TR/TE = 3000/ 10 ms, slice thickness = 3 mm, N_{Echoes} = 20, acquisition bandwidth = 200 Hz/Px]. Brain scans used a 16-channel receiver coil, pixel size = 1.1 $\times$ 1.1 mm^2, and matrix size = 192 $\times$ 150. Calf scans used a flexible 4-channel receive coil and 4 additional coils embedded in the scanner bed, with pixel size = 1.3 $\times$ 1.3 mm^2, and matrix size = 128 $\times$ 84.

3.2. Validation of L + S reconstruction models and identification of the fixed-rank parameter r

In order to validate the low-rank and sparse model of accelerated MESE data, we show that accurate qT$_2$ maps can still be generated from a low-rank version of the simulated EMC dictionary. T$_2$ and B$_1^+$ maps of scanned anatomy were generated by fitting the fully sampled data X against an SVD truncated versions of the EMC dictionary using a gradually decreasing number of singular values. Truncation was performed separately for each value of B$_1^+$, and maps were generated using the EMC algorithm for each level of truncation. These T$_2$ maps were then compared against the ground truth map generated from the full-rank EMC dictionary by calculating the mean and standard deviation (**SD**) of their relative errors (**RE**) according to

$$RE = 100 \bullet \frac{T_{2,ref} - \widehat{T_2}}{T_{ref}} \quad (4)$$

Here, $\widehat{T_2}$ is the T$_2$ value of voxels in the estimated map, and $T_{2,\ ref}$ is the T$_2$ value of voxels in the ground truth reference map. Finally, a fixed-rank r was chosen for SPARK reconstructions, equal to the minimal r value that showed no significant improvement in the SD of the relative error.

3.3. Data undersampling

Data were retrospectively undersampled at factors of $R = 2$ to 6. Pseudorandom non-uniform undersampling schemes were designed and applied along the phase encoding direction [28]. Different variable-density undersampling masks were used for each echo-time in the MESE series of images to produce an incoherent sampling patterns. Each mask was randomly generated using a power law probability density function (**PDF**) with parameter $p = 6$, as described by Lustig [28] and Knoll [36]. Such PDF reflects the power density spread in k-space, favoring high energy central lines over the k-space periphery.

Monte Carlo simulations were carried out to generate 600 different undersampling masks for each echo in the MESE echo-train, followed by selecting the optimal mask, i.e., the one which minimized the side-lobe to peak ratio (**SPR**) [28]. Calculation of the SPR was performed using the Point Spread Function (**PSF**) of the multicoil encoding operator E, as described in the SENSE algorithm [28,33,37]. We note that the design of undersampling masks necessitates the use of the coil sensitivity (B$_1^-$) maps. Since coil profiles are relatively similar for each specific anatomy, we calculated the undersampling masks only once per coil configuration and anatomy. Coil profiles were estimated from the fully sampled k-space data as a preprocessing stage by applying the adaptive coil combine algorithm by Walsh et al. [38] and dividing each profile by its maximum absolute value. Elaborate description for the derivation of the PSF and SPR used in this work is provided in Appendix B.

3.4. Image reconstruction

Fully sampled images were reconstructed using standard inverse-FT and adaptive coil combination. Retrospective undersampling of the k-space data was applied using the precalculated ETL set of masks, sorted by increasing SPR. Undersampled data were then reconstructed using two techniques: standard L + S (Eq. (1)), and the SPARK algorithm (Eq. (2) and Algorithm 1). In both cases, coil sensitivity profiles were calculated from 24 central fully sampled k-space lines, apodised with a Hann window of length 26. The coil profiles were divided by their maximum absolute value and a constant step size $t = 1$ was used. The magnitude of the k-space data was pre-normalized to a range [0,1] prior to the retrospective undersampling to enable choosing λ_L and λ_S from a constant dynamic range. The values of these weights were thus optimized using grid search over 20 possible values each, in the range 10^{-6} to 1. This optimization was performed by evaluation of the mean and SD

of the relative error with respect to the ground truth qT_2 map according to Eq. (4). Once λ_L and λ_S were determined, the undersampling scheme was once again optimized by examining 100 permutations of the undersampling patterns across the different echo times, applying the same optimization criterion. For SPARK reconstruction, a fixed rank value was set to $r = 7$ after inspecting the SVD of the EMC dictionary.

3.5. Generation of qT_2 maps – the EMC algorithm

T_2 maps were generated using the EMC algorithm once based on the fully sampled (ground truth) data, and once from the undersampled k-space data after applying the L + S, SPARK and GRAPPA reconstructions. EMC dictionary was generated for 21 equispaced B_1^+ values between 80% and 120% to incorporate inhomogeneities of the B_1^+ field, and 305 T_2 values logarithmically spaced between 5 and 1200 ms. Comprehensive description of the EMC fitting procedure can be found in [22].

3.6. Evaluating qT_2 mapping accuracy

Accuracy of qT_2 maps was estimated for all investigated anatomies. In brain scans, skull stripping was applied to exclude errors in the skull and sinuses areas [39]. Calf data were automatically segmented to remove the subcutaneous fat, skin, and bone marrow using a convolutional neural-network based segmentation [40,41]. Additional erosion of 1 voxel was subsequently applied to avoid partial volume effects. Regions of interest (**ROIs**) were manually delineated within each anatomy in order to evaluate the relative error in specific areas as shown in Fig. 1. For brain images, the head of caudate nucleus, putamen, thalamus, and splenium of corpus callosum were segmented. For calf images, the gastrocnemius, soleus, flexor longus, tibialis anterior, and peroneus longus muscles were segmented.

Relative errors were calculated per voxel by comparing the qT_2 maps, generated from the undersampled data, to the fully sampled (ground truth) qT_2 maps, according to Eq. (4). The mean and SD of the RE (MRE and SDRE relatively) were then calculated for each ROI. While T_2 values smaller than a single TE are too short to be estimated, T_2 values >180 ms are well above brain tissue values (excluding CSF), as well as muscle, fat, and bone marrow tissues in the calf. Pixels with $T_2 < TE$ or $180 > T_2$ ms in the fully sampled ground truth data were thus masked out and excluded from the error estimation.
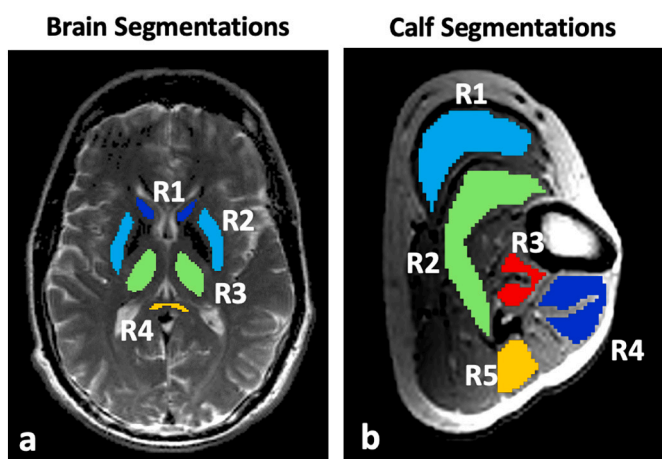
4. Results

Brain T_2 maps generated by fitting to an SVD truncated EMC dictionary using only the 4 largest singular values, with MRE and SDRE of 0.03% and 0.26% respectively. For the calf we found that using 6 singular values reduced the MRE and SDRE to 0.001% and 0.54% only. Assuming the experimental signals may require some higher rank to be well represented, we thus chose $r = 7$ to represent the EMC dictionary in the subsequent SPARK reconstruction of both anatomies.

Plots of MRE and SDRE against the number of singular values used for reconstruction are given as supplementary results (Fig. S1). The undersampling patterns for brain and for calf data were designed separately for L + S and for SPARK, seeing as the best undersampling pattern for SPARK is not necessarily the same as for L + S. Undersampling patterns for the brain data and SPARK reconstruction are shown in Fig. 2 for acceleration factors $R = 2$ to 6.

The full set of reconstruction parameters used for brain and calf will be supplied by request for both L + S and SPARK. Of note, SPARK reconstructions of the brain and calf were performed using a constant $\lambda_S = 0.1$ and $r = 7$ for all acceleration factors, thereby reducing the complexity of the parameter selection process.

T_2 maps of the brain and calf for acceleration factors x2, x4 and x6 are shown in Figs. 3-4. Image series were produced using three reconstruction techniques: GRAPPA, L + S and SPARK, with the final T_2 fitting performed using the EMC algorithm for all three techniques. As can be appreciated, all three techniques produce reasonable T_2 maps at standard acceleration factor of 2. Undersampling related artifacts appear, however, for the GRAPPA reconstruction at $R = 4$, 6 (appearing already at $R = 3$). L + S and SPARK, on the other hand, retain diagnostic quality even for x6 acceleration, attesting to the superiority of these approaches for reconstructing undersampled relaxation data.

Global error statistics are plotted against acceleration factor in Fig. 5 and Fig. 6 for brain and calf, respectively. As can be seen, the low rank techniques provide highly accurate T_2 maps with a close-to-zero mean error for almost all acceleration factors compared to GRAPPA whose
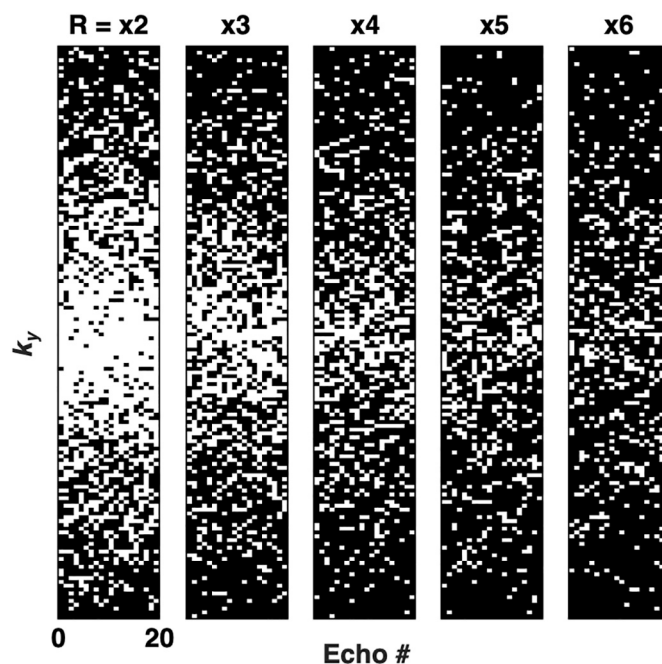

Fig. 1. Segmented regions of interest (ROIs), used for the evaluation of T_2 mapping performance. (a) Brain ROIs: R1, head of caudate nucleus; R2, putamen; R3, thalamus; R4, splenium of corpus callosum. (b) Calf ROIs: R1, gastrocnemius; R2, soleus; R3, flexor longus; R4, tibialis anterior; R5, peroneus longus muscle.

Fig. 2. Optimal undersampling patterns used for brain datasets and SPARK reconstruction at acceleration factors R = x2...x6. Patterns were identified using Monte-Carlo simulations and an SPR criterion. Optimization process resulted in a different set of undersampling masks for L + S reconstruction (not shown).
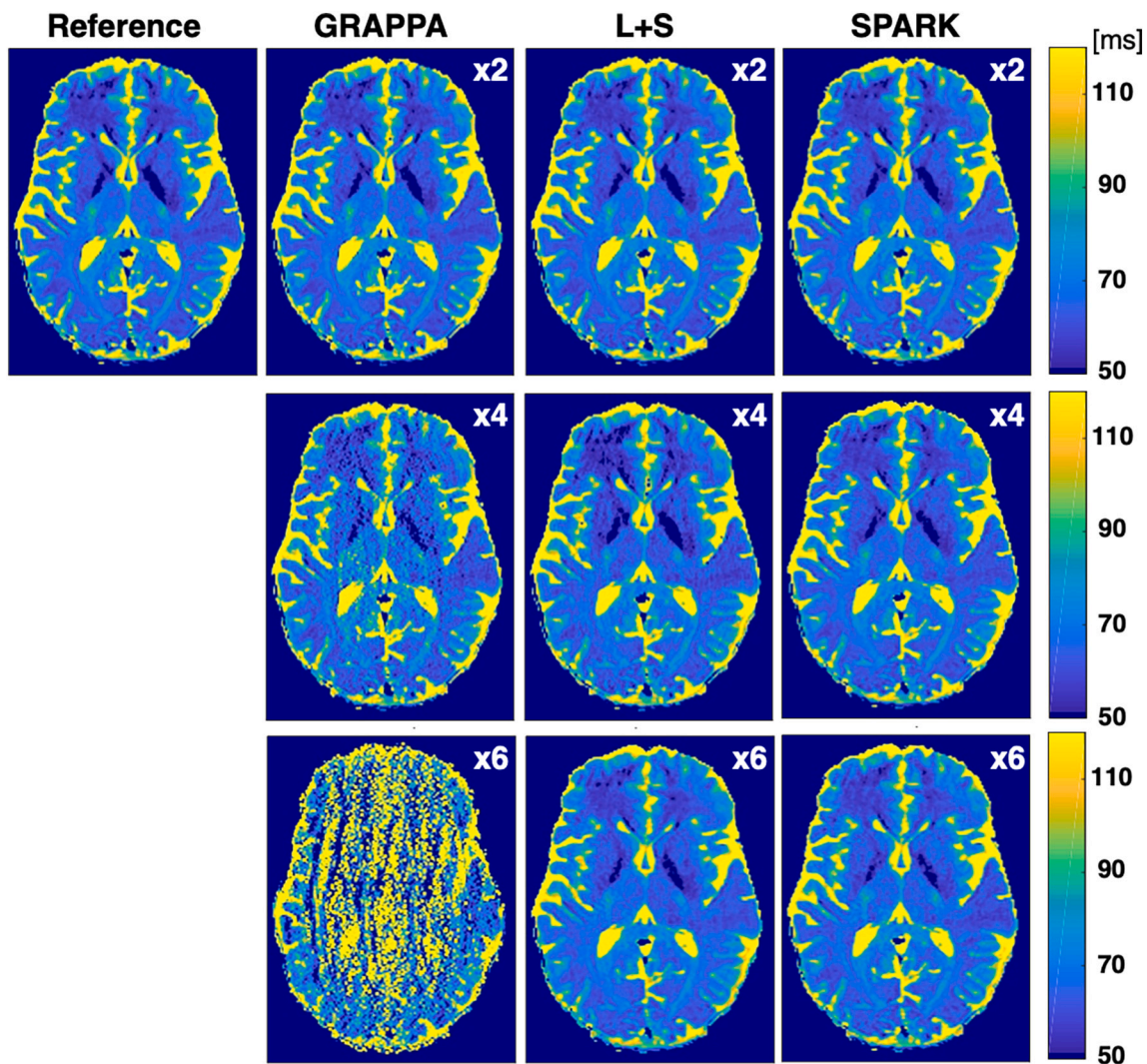
Fig. 3. Quantitative T_2 maps of the brain, reconstructed using GRAPPA, L + S, and SPARK in combination with the EMC algorithm. All methods show similar qT_2 mapping quality at $R = 2$. GRAPPA reconstruction, however, exhibits visible artifacts from $R = 4$ and above, while L + S and SPARK retain clinically acceptable accuracy even at $R = 6$ with no noticeable bias or artifacts. Reference qT_2 map was reconstructed from a fully sampled dataset.

accuracy decrease rapidly with R. SPARK and L + S brain qT_2 maps were unbiased by the undersampling, with a maximal average bias of around 1.8% and <0.6% for $R < 5$. The precision of these techniques is reflected in the error SD, which keeps a very moderate increase for L + S and SPARK, vs. GRAPPA. Similar results were obtained for the calf anatomy (Figs. 4 & 6), with a maximal bias below 1%.

Region-specific error statistics are presented in Tables 1 and 2 for brain and for calf, respectively. SPARK provides slightly better accuracy (lower SD), compared to L + S for most assayed ROIs, while both methods outperform standard GRAPPA.

5. Discussion

This work presents two new techniques for accelerating MESE acquisition of T_2 relaxation maps, with high undersampling of the *k*-t domain, and using the EMC fitting algorithm. Our findings suggest that acceleration can be successfully achieved using either the L + S or the SPARK algorithms. The EMC algorithm endows this mapping process with an additional layer of accuracy and stability by enabling the extraction of consistent values across scanners and scan settings [11,17]. Both L + S and SPARK require optimization of the reconstruction process in order to produce high T_2 mapping accuracy. Owing to the use of retrospective undersampling we were able to faithfully estimate the T_2

mapping accuracy and optimize the reconstruction parameters thereby evading the problems of visual inspection and lack of ground truth.

Looking beyond any similarity or discrepancy between the different low rank techniques, we emphasize that neither L + S [33] nor the PEAR technique (designed for accelerating fMRI acquisitions [34]) were previously used to accelerate the acquisition of quantitative T_2 relaxation maps. Thus, the novelty of SPARK lies in the way it incorporates the EMC signal model in the reconstruction process, both during pre- and post-processing stages. During preprocessing the EMC signal model is used to determine the MESE signal fixed rank, while during postprocessing the EMC qT2 mapping algorithm is used to generate accurate and stable T_2 maps from the reconstructed images.

Common measures for evaluating the performance of image reconstruction techniques are the Root Mean Squared Error (**RMSE**), the normalized RMSE (**nRMSE**), and the Structural Similarity (**SSIM**). While SSIM is indicative of the perceived image quality, low values of RMSE and nRMSE may not necessarily indicate visual similarity. Despite the popularity of these error estimates, we found the MRE and SDRE more appropriate for the task of evaluation of qT_2 quality, reflecting both the accuracy (bias) and precision (SD) of the estimated T_2 values. Moreover, we consider the calculation of MRE and SDRE more appropriate than the calculation of the average magnitude of the relative error. While the averaging of errors with opposite sign cancels the average RE, their SD
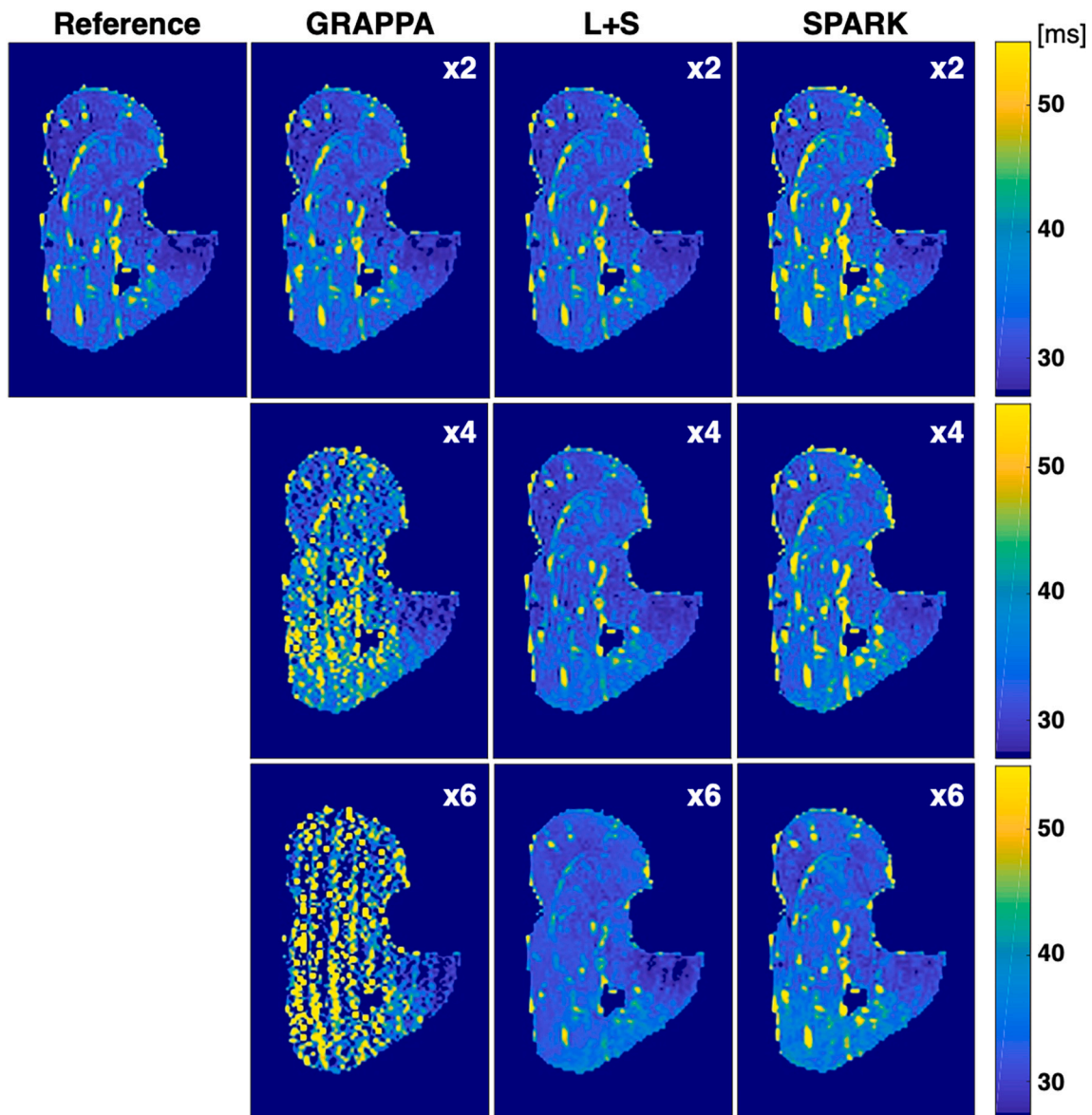
Fig. 4. Quantitative T_2 maps of the calf, reconstructed using GRAPPA, L + S, and SPARK in combination with the EMC algorithm. Bones and subcutaneous fat were automatically segmented out of the analyzed anatomy using a convolutional neural network [40,41]. All methods show similar reconstruction accuracy at R = 2. Maps reconstructed using GRAPPA show visible artifacts at R = 4 and above, while L + S and SPARK provide improved accuracy even at R = 6 with no noticeable bias or artifacts. Reference qT_2 map was reconstructed from a fully sampled dataset.
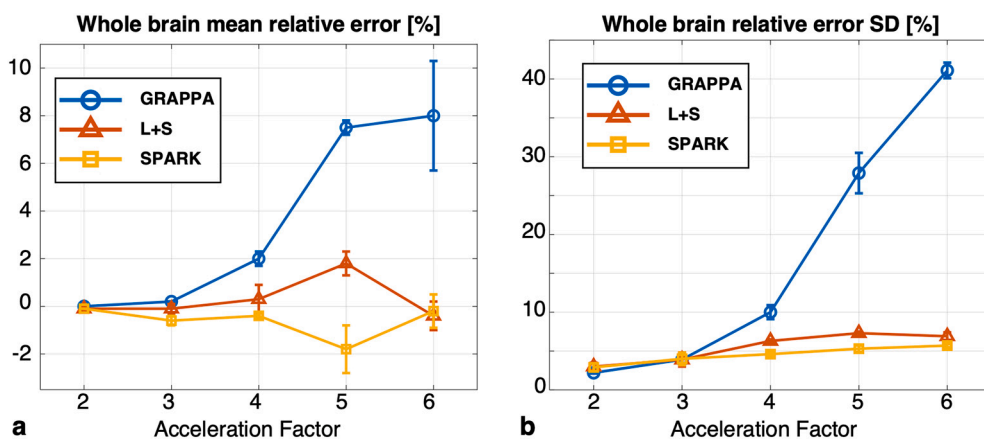

Fig. 5. Mean (a) and standard deviation (b) of the relative error in T_2 maps of the whole brain, averaged across the three brain datasets. Error levels were calculated across the brain soft tissue after skull stripping. Both L + S and SPARK are nearly unbiased, with mean relative errors below 0.6% for all acceleration factors other than $R = 5$ which produced error $\leq 2\%$. SD of all three methods remain below 4% at R = 2,3, with SPARK and L + S exhibiting improved performance vis-à-vis GRAPPA at higher acceleration factors. Vertical error bars denote inter-scan variability, calculated as the standard deviation between the three brain datasets, and exhibiting high inter-scan repeatability.
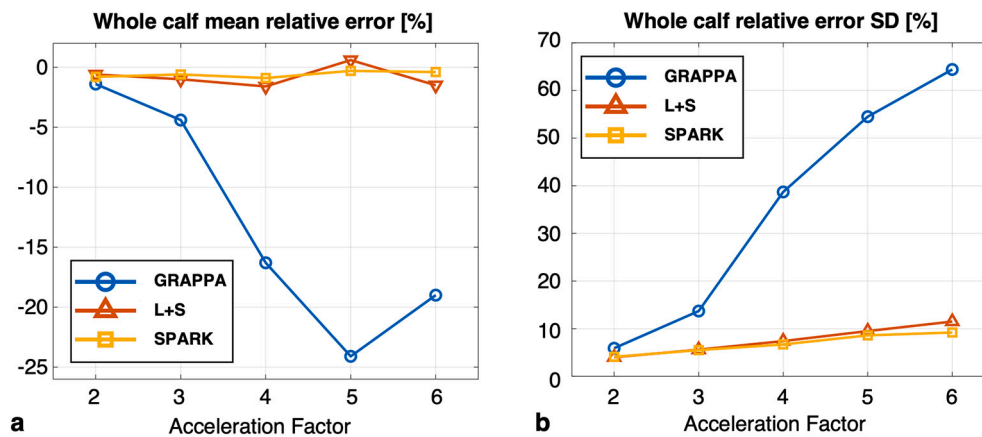
Fig. 6. Mean (a) and standard deviation (b) of the relative error in T$_2$ maps of the calf. Error values were calculated across the calf muscles, excluding the sub-cutaneous fat and the bones. Both L + S and SPARK are nearly unbiased, with mean relative errors below 1% for all acceleration factors. Precision (SD) of L + S and SPARK remain below 5.6% at R = 2, 3, and outperform GRAPPA at all acceleration factors.

Table 1
T$_2$ mapping accuracy (MRE) and precision (SDRE) for specific regions of interest in the brain, averaged across the three brain datasets [PU- putamen, HCN- head of caudate nucleus, TH- thalamus, SP- splenium].

ROI	Acceler. Factor →	x2	x3	x4	x5	x6
HCN	GRAPPA	−0.1 ± 2.0	0.2 ± 4.2	4.5 ± 12.5	19.2 ± 39.1	10.1 ± 49.2
	L + S	−0.3 ± 2.6	−0.1 ± 3.4	−0.1 ± 4.9	2.6 ± 5.8	1.1 ± 5.3
	SPARK	−0.3 ± 2.7	−0.7 ± 3.3	−0.9 ± 3.2	−1.3 ± 4.6	0.4 ± 4.3
PU	GRAPPA	−0.2 ± 2.7	0.5 ± 5.0	4.0 ± 13.2	16.9 ± 40.0	10.7 ± 49.9
	L + S	0.0 ± 3.0	0.7 ± 4.0	−0.7 ± 5.1	2.2 ± 5.7	0.2 ± 4.9
	SPARK	0.0 ± 2.7	−0.2 ± 3.8	−0.3 ± 3.5	−1.5 ± 4.4	1.5 ± 5.6
SP	GRAPPA	0.2 ± 2.5	0.5 ± 4.4	4.0 ± 12.0	7.6 ± 31.3	2.9 ± 41.7
	L + S	−0.3 ± 3.0	−0.1 ± 3.7	−1.1 ± 5.3	4.7 ± 5.4	−1.0 ± 5.0
	SPARK	−0.3 ± 2.7	−0.6 ± 3.9	−2.2 ± 4.0	−2.2 ± 5.6	−0.2 ± 5.4
TH	GRAPPA	0.0 ± 2.9	0.9 ± 5.8	5.4 ± 16.8	6.7 ± 38.5	3.3 ± 44.6
	L + S	−0.4 ± 3.4	−0.9 ± 4.6	−3.6 ± 4.8	−2.3 ± 6.1	−2.5 ± 5.0
	SPARK	−0.8 ± 3.4	−1.8 ± 4.9	−2.3 ± 4.4	−5.1 ± 4.9	−2.2 ± 5.8

Table 2
T$_2$ mapping accuracy (MRE) and precision (SDRE) for specific regions of interest in the calf [GM- gastrocnemius muscle, SM- soleus muscle, FL- flexor longus, PL-peroneus longus, TA- tibialis anterior].

ROI	Acceler. Factor →	x2	x3	x4	x5	x6
GM	GRAPPA	0.3 ± 3.4	2.6 ± 10.2	10.3 ± 28.3	29.0 ± 58.1	25.2 ± 69.8
	L + S	1.2 ± 2.9	1.2 ± 3.7	1.8 ± 5.0	1.3 ± 6.7	4.4 ± 8.4
	SPARK	0.6 ± 2.8	0.5 ± 4.1	2.0 ± 4.0	2.4 ± 5.4	1.3 ± 6.7
SM	GRAPPA	1.2 ± 5.8	3.1 ± 12.5	18.2 ± 40.6	18.9 ± 44.0	23.3 ± 74.2
	L + S	0.8 ± 4.0	0.7 ± 5.4	1.5 ± 6.6	−3.1 ± 8.2	0.8 ± 8.4
	SPARK	0.5 ± 3.8	−0.6 ± 5.0	0.8 ± 6.5	2.2 ± 6.7	−1.4 ± 7.7
FL	GRAPPA	0.7 ± 3.6	5.1 ± 17.8	10.2 ± 25.3	19.4 ± 47.2	20.3 ± 61.3
	L + S	1.5 ± 2.5	0.9 ± 3.8	0.3 ± 5.3	1.5 ± 6.4	2.8 ± 8.4
	SPARK	0.8 ± 2.7	0.8 ± 3.8	−0.3 ± 5.2	−1.0 ± 6.0	−1.5 ± 6.1
PL	GRAPPA	0.6 ± 2.6	8.1 ± 10.8	18.4 ± 27.4	31.2 ± 63.6	22.2 ± 63.8
	L + S	1.5 ± 2.8	0.9 ± 4.0	5.1 ± 7.1	6.0 ± 9.6	6.6 ± 11.0
	SPARK	1.3 ± 2.6	2.8 ± 3.4	2.6 ± 4.8	−7.4 ± 5.2	3.4 ± 7.7
TA	GRAPPA	0.2 ± 2.7	0.9 ± 4.6	2.5 ± 9.7	8.5 ± 23.1	2.6 ± 21.6
	L + S	1.0 ± 2.9	2.1 ± 3.2	2.6 ± 4.7	−0.5 ± 6.9	3.1 ± 7.5
	SPARK	0.7 ± 2.4	0.6 ± 4.1	1.4 ± 4.5	−0.7 ± 5.7	3.0 ± 4.7

would increase due to their signs. In contrary, averaging the magnitude of the RE would not supply information about any bias in the estimated values.

Though phantoms are commonly used to validate the accuracy of T$_2$ values, in this work we relied on the validity and accuracy of the EMC algorithm [1]. Hence, model validations used retrospective undersampling, while using the T$_2$ maps generated from fully sampled data as ground truth. Employing prospective undersampling will require the collection of three separate datasets, acquired during three separate scans, seeing as each reconstructed technique has its own optimal undersampling scheme. This would have introduced an inter-scan variability, which would contaminate the comparison against a fully sampled reference scan. Retrospective undersampling, on the other hand, allowed us to accurately compare between methods, where different undersampling schemes and reconstruction methods are applied on the exact same dataset. Thus, any variability between T$_2$ maps was attributed to the difference between reconstruction models

alone, without natural inter scan variability due to motion or noise. Further validations are required using prospective undersampling, although such acquisitions are expected to produce even higher mapping accuracy, as they will be less susceptible to motion artifacts due to their shorter acquisition times.

The standard approach for designing undersampling masks for L + S is based on the selection of ETL different patterns, randomly undersampling the phase-encoding dimension. These patterns are designed so as to maximize the incoherence between undersampling-related aliasing artifacts [28,33]. Although undersampling techniques tailored for L + S reconstructions were not found in the literature during this work, many similar techniques were previously developed for CS-MRI. Most of these

works evaluate the undersampling schemes by assessing the quality of the reconstructed training data. Such evaluation approach requires prior knowledge regarding the regularization parameters values, which are not always known and depend on the undersampling scheme itself. Furthermore, a criterion for assessing the quality of the final image is also needed. Using the SPR criterion we avoided both problems since image reconstruction was not required.

The PSF of the acquisition operator E, can be formulated as a block-diagonal square matrix, where each block is the PSF of the multi-coil acquisition of a single echo (see Appendices A and B). Theoretically, this makes the SPR of E insensitive to the order of the undersampling patterns. Consequently, the SPR will be the maximum amongst all echoes. Nonetheless, we found the temporal arrangement of undersampling patterns to have a significant effect on the qT_2 mapping performance, mainly at acceleration factors >3.

The design of undersampling schemes based on the SPR criterion makes use of the coil sensitivities for the calculation of the PSF. Reconstruction of prospectively undersampled data might encounter some variability in the coil sensitivity profiles, resulting in different SPR values than the ones found during the scheme design. This, however, is not expected to become a limitation since the sampling patterns are designed per anatomy and coil configuration. The estimation of the coil sensitivities from few fully sampled central k-space lines is done as a preprocessing stage prior to image reconstruction. This approach assumes that most of the k-space data is concentrated in its low frequencies. The selection of such lines is thus similar to applying a rectangular low-pass filter. Such filters are characterized by relatively large side-lobes, which caused significant artifacts in the estimated coil sensitivity maps. Apodizing these central lines with a Hann window significantly reduced the side-lobes magnitude and resulting artifacts, thereby improving the T_2 maps quality.

Global optimization of reconstruction parameters for L + S and SPARK may be a difficult and probably intractable task. In this study, we adopted a greedy approach to solve this task, which, although time consuming, led to satisfactory results. Using grid search for the selection of λ_S and λ_L, we found that SPARK is more robust than L + S to different regularization values, resulting in a larger range of parameter values achieving optimal or near optimal T_2 mapping performance and alleviated the constraints on parameter selection. Our results show that using $\lambda_S = 0.1$ in SPARK at all acceleration factors and for both datasets yields similar results to those achieved using an exhaustive 2D grid search.

Theoretical analysis of the EMC dictionary's singular values showed that it can be well-approximated using a rank of $r \geq 4$–5. From a practical point of view, however, we assumed the experimental rank to be higher than the theoretical one due to noise and other imperfections. Hence, we set the rank at a fixed value of $r = 7$ for SPARK, which, in most cases, was enough to outperform L + S given a suitable pair of $[\lambda_S, \lambda_L]$ values. Moreover, the undersampling schemes and reconstruction parameters of the brain scans were based on a single dataset per anatomy

and applied for the remaining datasets. These results attest to the robustness of the postprocessing approach across similar anatomies.

Our results show that brain T_2 maps have reduced SDRE compared to the calf maps. We found that large relative errors in brain T_2 maps are prone to occur at the edges of our stripped skull, and simple erosion of the binary segmentation mask reduced the mean and SD of the RE (Fig. S2). Nonetheless, large relative errors in calf appear not only at partial volume voxels, but also in the center of the anatomy, and are related to blood circulation.

L + S was originally applied as a method for acceleration of dynamic MRI based on foreground / background signal separation, where L contains mainly background data and S contains the signal of interest, which is sparse in some transform domain. Perfusion data, for example, used temporal FT as a sparse transform, while angiography data employed the Identity transform for S, representing sparsity in the image domain. Another example is the PEAR technique [34], in which the signal was modeled as composed of both periodic and wideband components, so that both L and S contain signals of interest. In SPARK, the low rank property of MESE signals, and the corresponding EMC dictionary of theoretical signals, enables modeling the signal of interest as L while using S to eliminate residual aliasing-related noise, which is sparse in the image domain.

The main difference between SPARK and L + S lies in the SVT mechanism used for the solution of the L-step. Whereas L + S solves L by applying SVT on its singular values with parameter $\lambda_L \bullet \sigma_1$, SPARK applies SVT with parameter $\lambda_L \bullet \sigma_{r+1}$, followed by rank truncation to the fixed-rank r [34,35].

6. Conclusions

This work presented the application of two new reconstruction techniques, L + S and SPARK, for accurate mapping of T_2 relaxation values from accelerated MESE data. We show that the low or fixed rank and sparsity-based models provide sufficient accuracy at acceleration factors ≥3, significantly overperforming standard GRAPPA. SPARK exhibits small improvement over L + S in terms of T_2 mapping accuracy, while demonstrating a significantly improved robustness to rank-selection and to regularization parameters' values. This property may contribute to future application of SPARK, enabling the acquisition of highly accelerated MESE data and facilitating the use of quantitative T_2 in clinical settings.

Declaration of Competing Interest

Authors have nothing to disclose.

Acknowledgments

Appendix A. Definition of the encoding operator (E)

Let $x_i \in \mathbb{R}^{N_x N_y}$ be the column-stacked i-th echo in a MESE signal of ETL echoes, and let $y_i^{(j)} \in \mathbb{C}^{N_{kx} N_{ky}}$ be the column-stacked k-space data acquired at the j-th coil from signal x_i using the encoding operator $E_i^{(j)} = U_j F C^{(j)}$

$$y_i^{(j)} = E_i^{(j)} x_i \tag{A1}$$

The coils sensitivity map $C^{(j)} \in \mathbb{C}^{N_x N_y \times N_x N_y}$ is a complex diagonal matrix performing element-wise multiplication of voxels in x_i, and the undersampling pattern $U_i \in \mathbb{R}^{N_{kx} N_{ky} \times N_{kx} N_{ky}}$ is a diagonal matrix with 1's at sampled k-space voxels and 0 elsewhere. F is the 2D FT matrix operating on the vectorized echo.

The parallel acquisition of k-space in N_{coils} at the i-th echo, $y_i \in \mathbb{C}^{N_{kx} N_{ky} N_{coils}}$, is the concatenation of Eq. (A1) N_{coils} times, acquired by E_i. Since same undersampling is performed for all coils during the same echo, $y_i = E_i x_i$ can be written as

$$y_i = \begin{bmatrix} U_i & & & \\ & U_i & & \\ & & \ddots & \\ & & & U_i \end{bmatrix} \begin{bmatrix} F & & & \\ & F & & \\ & & \ddots & \\ & & & F \end{bmatrix} \begin{bmatrix} C^{(1)} \\ C^{(2)} \\ \vdots \\ C^{(N_{coils})} \end{bmatrix} \tag{A2}$$

In the same way we derive the multi-echo sequence of parallel acquisitions $y \in \mathbb{C}^{N_{kx}N_{ky}N_{coils}ETL}$, acquired by E from signal $x \in \mathbb{R}^{N_xN_yETL}$, concatenating Eq. (A2) ETL times. Eq. A3 represents the acquired k-space of the multi-coil MESE signal, denoted as $y = Ex$.

$$\begin{bmatrix} y_1 \\ y_2 \\ \vdots \\ y_{ETL} \end{bmatrix} = \begin{bmatrix} E_1 & & & \\ & E_2 & & \\ & & \ddots & \\ & & & E_{ETL} \end{bmatrix} \begin{bmatrix} x_1 \\ x_2 \\ \vdots \\ x_{ETL} \end{bmatrix} \tag{A3}$$

Appendix B. Definition of PSF and SPR

The point spread function (**PSF**) and side-lobe to peak ratio (**SPR**) of E are defined by

$$PSF_{ij} = e_j^* E^* E e_i \tag{B1}$$

$$SPR = \max_{i \neq j} PSF_{ij} \tag{B2}$$

where E is the encoding operator and $e_i \in \mathbb{R}^{N_xN_yETL}$ is equal to 1 at voxel i and 0 elsewhere. From Eq. (A3) in Appendix A we see that

$$E^*E = \begin{bmatrix} E_1^*E_1 & & & \\ & E_2^*E_2 & & \\ & & \ddots & \\ & & & E_{ETL}^*E_{ETL} \end{bmatrix} \tag{B3}$$

From Eq. (B3) it is clear that E does not induce correlations between the echoes and the PSF of each echo can be calculated separately. Moreover, the SPR of E is the maximum off-diagonal absolute value in the PSF. Since E^*E is block-diagonal, the SPR of E is the maximum SPR of all echoes.

The value in the j-th voxel of the k-th echo is given by

$$e_{kj}^* E_k^* E_k e_{ki} = e_{kj}^* F^* U_k F e_{ki} \sum_{l=1}^{N_{coils}} c_j^{(l)*} c_i^{(l)} \tag{B4}$$

From Eq. (B4) we can see that when coil sensitivity maps are not constant, they will influence the calculation of the SPR of E.

Appendix C. Supplementary data

Supplementary data to this article can be found online at https://doi.org/10.1016/j.mri.2023.01.007.

References

[1] Ben-Eliezer N, Sodickson DK, Block KT. Rapid and accurate T2 mapping from multi-spin-echo data using bloch-simulation-based reconstruction. Magn Reson Med 2015;73(2):809–17. https://doi.org/10.1002/mrm.25156.

[2] Gracien RM, Maiworm M, Brüche N, et al. How stable is quantitative MRI? – assessment of intra- and inter-scanner-model reproducibility using identical acquisition sequences and data analysis programs. Neuroimage. 2020;207:116364. https://doi.org/10.1016/j.neuroimage.2019.116364.

[3] Tofts P, editor. Quantitative MRI of the brain. Chichester, UK: John Wiley & Sons, Ltd; 2003. https://doi.org/10.1002/0470869526.

[4] Farraher SW, Jara H, Chang KJ, Ozonoff A, Soto JA. Differentiation of hepatocellular carcinoma and hepatic metastasis from cysts and hemangiomas with calculated T2 relaxation times and the T1/T2 relaxation times ratio. J Magn Reson Imaging 2006;24(6):1333–41. https://doi.org/10.1002/jmri.20758.

[5] Liu W, Turkbey B, Sénégas J, et al. Accelerated T2 mapping for characterization of prostate cancer. Magn Reson Med 2011;65(5):1400–6. https://doi.org/10.1002/mrm.22874.

[6] Jordan CD, Saranathan M, Bangerter NK, Hargreaves BA, Gold GE. Musculoskeletal MRI at 3.0 T and 7.0 T: a comparison of relaxation times and image contrast. Eur J Radiol 2013;82(5):734–9. https://doi.org/10.1016/j.ejrad.2011.09.021.

[7] Pan J, Pialat J-B, Joseph T, et al. Knee cartilage T2 characteristics and evolution in relation to morphologic abnormalities detected at 3-T MR imaging: a longitudinal study of the Normal control cohort from the osteoarthritis initiative. Radiology. 2011;261(2):507–15. https://doi.org/10.1148/radiol.11102234.

[8] Mosher TJ, Zhang Z, Reddy R, et al. Knee articular cartilage damage in osteoarthritis: analysis of MR image biomarker reproducibility in ACRIN-PA 4001 multicenter trial. Radiology. 2011;258(3):832–42. https://doi.org/10.1148/radiol.10101174.

[9] Dardzinski BJ, Mosher TJ, Li S, Van Slyke MA, Smith MB. Spatial variation of T2 in human articular cartilage. Radiology. 1997;205:546–50. https://doi.org/10.1148/radiology.205.2.9356643.

[10] Siemonsen S, Mouridsen K, Holst B, et al. Quantitative T2 values predict time from symptom onset in acute stroke patients. Stroke. 2009;40(5):1612–6. https://doi.org/10.1161/STROKEAHA.108.542548.

[11] Shepherd TM, Kirov II, Charlson E, et al. New rapid, accurate T2 quantification detects pathology in normal-appearing brain regions of relapsing-remitting MS patients. NeuroImage Clin 2017;14:363–70. https://doi.org/10.1016/J.NICL.2017.01.029.

[12] Cury RC, Shash K, Nagurney JT, et al. Cardiac magnetic resonance with T2-weighted imaging improves detection of patients with acute coronary syndrome in the emergency department. Circulation. 2008;118(8):837–44. https://doi.org/10.1161/CIRCULATIONAHA.107.740597.

[13] Eitel I, Friedrich MG. T2-weighted cardiovascular magnetic resonance in acute cardiac disease. J Cardiovasc Magn Reson 2011;13(1):13. https://doi.org/10.1186/1532-429X-13-13.

[14] Ben-Eliezer N, Sodickson DK, Shepherd T, Wiggins GC, Block KT. Accelerated and motion-robust in vivo T 2 mapping from radially undersampled data using bloch-simulation-based iterative reconstruction. Magn Reson Med 2016;75(3):1346–54. https://doi.org/10.1002/mrm.25558.

[15] Lebel RM, Wilman AH. Transverse relaxometry with stimulated echo compensation. Magn Reson Med 2010;64(4):1005–14. https://doi.org/10.1002/mrm.22487.

[16] McPhee KC, Wilman AH. Limitations of skipping echoes for exponential T 2 fitting. J Magn Reson Imaging 2018;48(5):1432–40. https://doi.org/10.1002/jmri.26052.

[17] McPhee KC, Wilman AH. Transverse relaxation and flip angle mapping: evaluation of simultaneous and independent methods using multiple spin echoes. Magn Reson Med 2017;77(5):2057–65. https://doi.org/10.1002/mrm.26285.

[18] Schmitt P, Griswold MA, Jakob PM, et al. Inversion recovery TrueFISP: quantification of T1, T 2, and spin density. Magn Reson Med 2004;51(4):661–7. https://doi.org/10.1002/mrm.20058.

[19] Deoni SCL, Peters TM, Rutt BK. High-resolution T1 and T2 mapping of the brain in a clinically acceptable time with DESPOT1 and DESPOT2. Magn Reson Med 2005; 53(1):237–41. https://doi.org/10.1002/mrm.20314.

[20] Hennig J. Multiecho imaging sequences with low refocusing flip angles. J Magn Reson 1988;78(3):397–407. https://doi.org/10.1016/0022-2364(88)90128-X.

[21] Ma D, Gulani V, Seiberlich N, et al. Magnetic resonance fingerprinting. Nature. 2013;495(7440):187–92. https://doi.org/10.1038/nature11971.

[22] Radunsky D, Stern N, Nassar J, Tsarfaty G, Blumenfeld-Katzir T, Ben-Eliezer N. Quantitative platform for accurate and reproducible assessment of transverse (T2) relaxation time. NMR Biomed 2021;34(8). https://doi.org/10.1002/NBM.4537.

[23] Radunsky D, Blumenfeld-Katzir T, Volovyk Osnat, et al. Analysis of magnetization transfer (MT) influence on quantitative mapping of T 2 relaxation time. Magn Reson Med 2019;82:145. https://doi.org/10.1002/mrm.27704.

[24] Chhetri G, Mcphee KC, Wilman AH. Bloch modelling enables robust t2 mapping using retrospective proton density and t2- weighted images from different vendors and sites. 2020. p. 19–21.

[25] Shpringer G, Bendahan D, Ben-Eliezer N. Accelerated reconstruction of dictionary-based T2 relaxation maps based on dictionary compression and gradient descent search algorithms. Magn Reson Imaging 2022;87:56–66. https://doi.org/10.1016/J.MRI.2021.12.006.

[26] Pruessmann KP, Weiger M, Scheidegger MB, Boesiger P. SENSE: sensitivity encoding for fast MRI. Magn Reson Med 1999;42(5):952–62. https://doi.org/10.1002/(SICI)1522-2594(199911)42:5<952::AID-MRM16>3.0.CO;2-S.

[27] Griswold MA, Jakob PM, Heidemann RM, et al. Generalized autocalibrating partially parallel acquisitions (GRAPPA). Magn Reson Med 2002;47(6):1202–10. https://doi.org/10.1002/mrm.10171.

[28] Lustig M, Donoho D, Pauly JM. Sparse MRI: the application of compressed sensing for rapid MR imaging. Magn Reson Med 2007;58(6):1182–95.

[29] Doneva M, Börnert P, Eggers H, Stehning C, Sénégas J, Mertins A. Compressed sensing reconstruction for magnetic resonance parameter mapping. Magn Reson Med 2010;64(4):1114–20. https://doi.org/10.1002/mrm.22483.

[30] Trzasko J, Manduca A. Local versus global low-rank promotion in dynamic MRI series reconstruction. Proc Int Soc Magn Reson Med 2011;24(7):4371.

[31] Zhang T, Pauly JM, Levesque IR. Accelerating parameter mapping with a locally low rank constraint. Magn Reson Med 2015;73(2):655–61. https://doi.org/10.1002/mrm.25161.

[32] Zhao B, Lu W, Hitchens TK, Lam F, Ho C, Liang ZP. Accelerated MR parameter mapping with low-rank and sparsity constraints. Magn Reson Med 2015;74(2): 489–98. https://doi.org/10.1002/mrm.25421.

[33] Otazo R, Candès E, Sodickson DK. Low-rank plus sparse matrix decomposition for accelerated dynamic {MRI} with separation of background and dynamic components. Magn Reson Med 2014;73(3):1125–36. https://doi.org/10.1002/mrm.25240.

[34] Weizman L, Miller KL, Eldar YC, Chiew M. PEAR: PEriodic and fixed rank separation for fast fMRI: PEriodic. Med Phys 2017;44(12):6166–82. https://doi.org/10.1002/mp.12599.

[35] Goldfarb D, Ma S. Convergence of fixed-point continuation algorithms for matrix rank minimization. Found Comput Math 2011;11(2):183–210. https://doi.org/10.1007/s10208-011-9084-6.

[36] Knoll F, Clason C, Diwoky C, Stollberger R. Adapted random sampling patterns for accelerated MRI. Magn Reson Mater Physics, Biol Med 2011;24(1):43–50. https://doi.org/10.1007/s10334-010-0234-7.

[37] Pruessmann KP, Weiger M, Börnert P, Boesiger P. Advances in sensitivity encoding with arbitrary k-space trajectories. Magn Reson Med 2001;46(4):638–51. https://doi.org/10.1002/mrm.1241.

[38] Walsh DO, Gmitro AF, Marcellin MW. Adaptive reconstruction of phased array MR imagery. Magn Reson Med 2000;43(5):682–90.

[39] Roy S, Maji P. A simple skull stripping algorithm for brain MRI. In: 2015 Eighth international conference on advances in pattern recognition (ICAPR). IEEE; 2015. p. 1–6. https://doi.org/10.1109/ICAPR.2015.7050671.

[40] Amer R, Nassar J, Bendahan D, Greenspan H, Ben-Eliezer N. Automatic segmentation of muscle tissue and inter-muscular fat in thigh and calf MRI images. In: Lecture notes in computer science (including subseries lecture notes in artificial intelligence and lecture notes in bioinformatics). Vol 11765 LNCS. Springer; 2019. p. 219–27. https://doi.org/10.1007/978-3-030-32245-8_25.

[41] Amer R, Nassar J, Trabelsi A, Bendahan D, Greenspan H, Ben-Eliezer N. Quantification of intra-muscular adipose infiltration in calf/thigh MRI using fully and weakly supervised semantic segmentation. Bioengineering. 2022;9(7):315. https://doi.org/10.3390/bioengineering9070315.